3D PRINTING

Volumetric additive manufacturing of silica glass with microscale computed axial lithography

Joseph T. Toombs[1]*, Manuel Luitz[2], Caitlyn C. Cook[3], Sophie Jenne[2], Chi Chung Li[1], Bastian E. Rapp[2,4,5,6], Frederik Kotz-Helmer[2,4,5], Hayden K. Taylor[1]*

Glass is increasingly desired as a material for manufacturing complex microscopic geometries, from the micro-optics in compact consumer products to microfluidic systems for chemical synthesis and biological analyses. As the size, geometric, surface roughness, and mechanical strength requirements of glass evolve, conventional processing methods are challenged. We introduce microscale computed axial lithography (micro-CAL) of fused silica components, by tomographically illuminating a photopolymer-silica nanocomposite that is then sintered. We fabricated three-dimensional microfluidics with internal diameters of 150 micrometers, free-form micro-optical elements with a surface roughness of 6 nanometers, and complex high-strength trusses and lattice structures with minimum feature sizes of 50 micrometers. As a high-speed, layer-free digital light manufacturing process, micro-CAL can process nanocomposites with high solids content and high geometric freedom, enabling new device structures and applications.

The uses of glass are innumerable because of its optical transparency, thermal and chemical resistance, and low coefficient of thermal expansion. Established applications in architecture, consumer products, optical systems, and art have been joined by specialized uses such as fiber optics in communication, diffractive optics in augmented reality, and lab-on-a-chip devices for chemical and biological analyses (*1*–*3*). With increased specialization come more demanding requirements for geometry, size, and optical and mechanical properties. Additive manufacturing (AM) has emerged as a promising technique to meet challenging new combinations of requirements. AM of glass materials has been achieved with fused filament fabrication of molten glass (*4*, *5*), selective laser melting of pure glass powder (*6*, *7*), direct ink writing of silica sol-gel inks (*8*), stereolithography (SLA) (*9*–*11*), and multiphoton direct laser writing (DLW) (*12*) of silica nanocomposites that consist of silica nanoparticles dispersed in a photopolymerizable organic liquid.

All these methods use serial material deposition or conversion, which can limit geometric freedom. Layering-induced defects can also affect the printed object's optical and mechanical properties (*5*, *13*). We introduce volumetric AM (VAM) of glass nanocomposites. VAM describes techniques that polymerize whole three-dimensional (3D) objects simultaneously in a volume of precursor material, circumventing the need to build objects layer by layer. VAM methods based on holographic exposure (*14*), orthogonal superposition (*15*), and tomographic principles (*16*, *17*) are enabled by specialized optical engineering and photopolymer synthesis. The tomographic technique of computed axial lithography (CAL) polymerizes 3D structures by the azimuthal superposition of iteratively optimized light projections from temporally multiplexed exposures (Fig. 1A) (*16*, *18*, *19*). CAL has several advantages for processing glass nanocomposites. No relative motion occurs between the precursor material and the fabricated object during printing, so high-viscosity and thixotropic nanocomposite precursors can easily be used. The layerless nature of the process enables smooth surfaces and complex geometries. Because the fabricated object is surrounded by precursor material during printing, sacrificial solid supporting structures are not needed. These attributes are desirable for applications that include micro-optical components and microfluidics.

We sought the production of microscale features, so we constructed a "micro-CAL" apparatus (Fig. 1B) that coupled a laser light source into an optical fiber with small mode field size and low numerical aperture (*17*) and demagnified the light pattern defined by the digital micromirror device. This design minimized the system's étendue and hence the divergence and blurring of light. We measured optical resolution in terms of the modulation transfer function (MTF), which is the level of contrast transfer by the complete optical system as a function of spatial frequency. We achieved an MTF greater than 0.4 at frequencies ≥66.7 cycles mm^{-1} in the central 1.5-mm diameter of the build volume (Fig. 1, D and E, and figs. S2 to S4). Combined with gradient descent digital mask optimization (*16*), the micro-CAL system enabled rapid printing (within about 30 to 90 s) of microstructures with minimum feature sizes of 20 and 50 μm in polymer and fused silica glass, respectively.

For the fused silica prints, we used a photocurable micro-stereolithography (μSL) v2.0 nanocomposite with high transparency (Fig. 2A) consisting of a liquid monomeric photocurable binder matrix and 35 vol % solid amorphous spherical silica nanoparticles with a nominal diameter of 40 nm. The high–solids content nanocomposite had a zero shear viscosity of 10 Pa·s at 23°C, and it exhibited thixotropic shear-thinning properties at moderate shear rates (1 to 100 s^{-1}) and shear-thickening properties at high shear rates (>100 s^{-1}) (*20*). The binder was polymerized via free-radical polymerization and supported the nanoparticles in the printed construct. After printing, we removed structures from the volume of nanocomposite and reused surplus nanocomposite for later prints. We developed the structures by rinsing in ethanol or propylene glycol methyl ether acetate for about 10 min to remove excess uncured nanocomposite. Heating up to 60°C was applied to reduce viscosity by up to an order of magnitude to assist in the development of small features. We subjected the resulting green parts to thermal treatment in two steps: debinding and sintering (Fig. 1A and tables S3 and S4). The debinding treatment burned out the polymer binder matrix, resulting in a porous silica brown part. During sintering, the nanoparticles of the brown part fused together, forming a dense transparent glass part. An isotropic linear shrinkage (fig. S8) of 26% occurred during sintering, which was consistent with the theoretical shrinkage predicted by thermogravimetric analysis, so it was necessary for us to scale parts in computer-aided design before fabrication to account for the dimensional change (*20*).

The tomographic illumination process of CAL means that material that is outside the target geometry receives an appreciable light dose. To achieve selective material conversion, the resin precursor therefore has a threshold light exposure dose below which polymerization is negligible. In prior VAM research, the induction period—the period of time in which conversion is inhibited by radical scavenger species in the resin—was a result of oxygen inhibition (*15*–*17*). However, the glass nanocomposite used in this work exhibited a small natural induction period. Besides molecular oxygen, several molecules—including quinones and nitroxides, such as 2,2,6,6-tetramethylpiperidinoxyl (TEMPO)—are recognized as effective radical inhibitors (*21*, *22*). We added various concentrations of TEMPO to the nanocomposite and performed real-time ultraviolet (UV) Fourier transform infrared spectroscopy (FTIR) analysis to determine the effect of TEMPO concentration on the inhibition time (Fig. 2B). The addition of TEMPO increased the duration of the induction period

[1]Department of Mechanical Engineering, University of California, Berkeley, CA 94720, USA. [2]Department of Microsystems Engineering, Albert Ludwig University of Freiburg, 79104 Freiburg, Germany. [3]Lawrence Livermore National Laboratory, Livermore, CA 94550, USA. [4]Glassomer GmbH, Georges-Köhler-Allee 103, 79110 Freiburg, Germany. [5]Freiburg Materials Research Center (FMF), Albert Ludwig University of Freiburg, 79104 Freiburg, Germany. [6]Freiburg Center of Interactive Materials and Bioinspired Technologies (FIT), Albert Ludwig University of Freiburg, 79110 Freiburg, Germany.
*Corresponding author. Email: jtoombs@berkeley.edu (J.T.T.); hkt@berkeley.edu (H.K.T.)

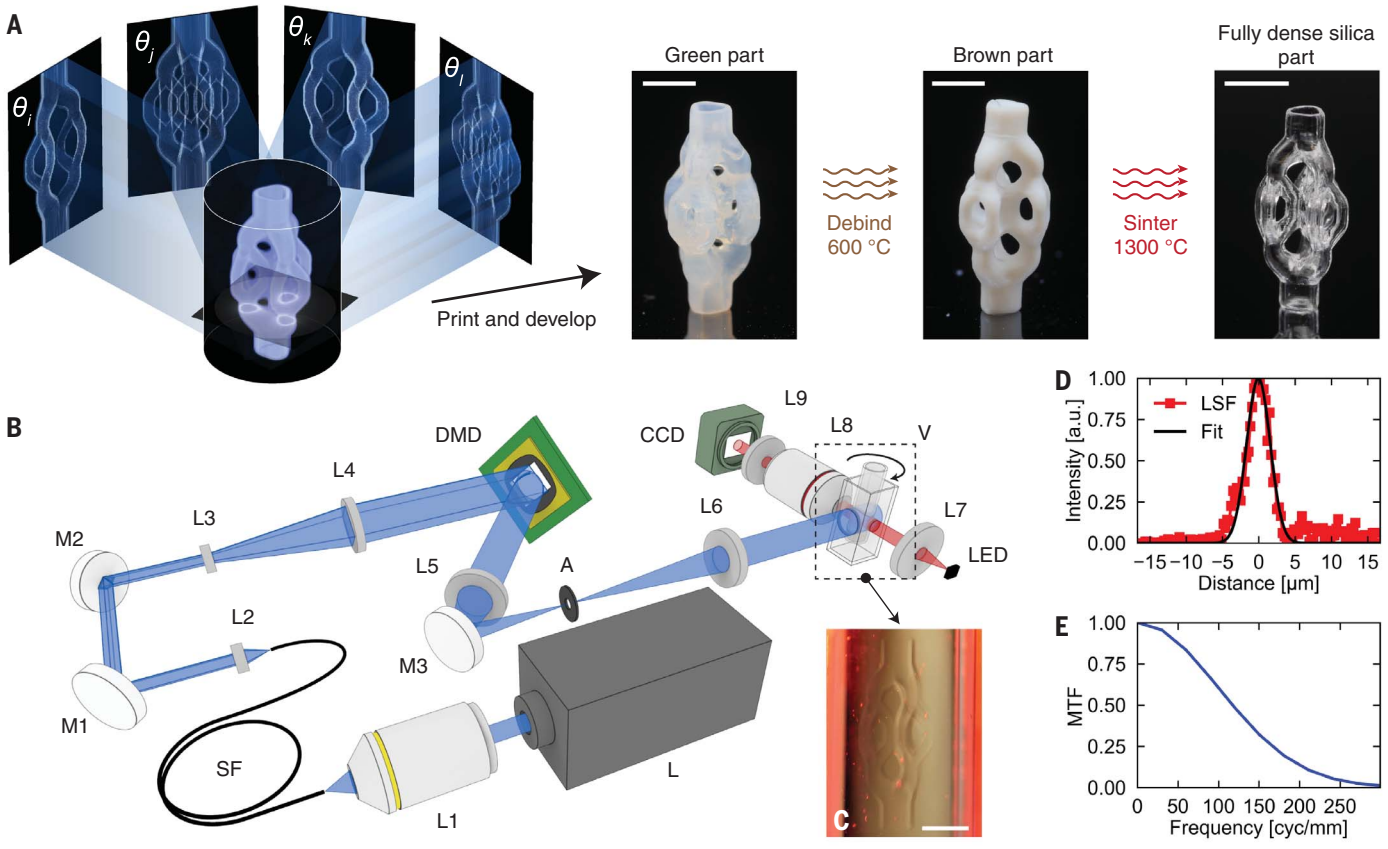

Fig. 1. Printing transparent fused silica glass with micro-CAL. (**A**) Tomographic superposition produces a 3D light dose that selectively polymerizes a geometry. After printing, the part is developed by rinsing away residual nanocomposite in a solvent. Debinding and sintering steps follow. Scale bars are 2 mm. θ_i to θ_l, examples of optimized tomographic digital light projections. (**B**) Optomechanical setup. A detailed description of the setup and components are given in (*20*). A, aperture; CCD, charge-coupled device; DMD, digital micromirror device; L, 3-W, 442-nm laser diode; L1 to L9, lenses 1 to 9; LED, light-emitting diode; M1 to M3, mirrors 1 to 3; SF, multimode square core fiber; V, print container. (**C**) Immediately after light exposure, the printed object can be observed in the container, weakly distorting the background. Scale bar is 2.5 mm. (**D** and **E**) Line spread function (LSF) (D) and MTF (E) at the focal plane of the micro-CAL system. a.u., arbitrary units; cyc/mm, cycles per millimeter.

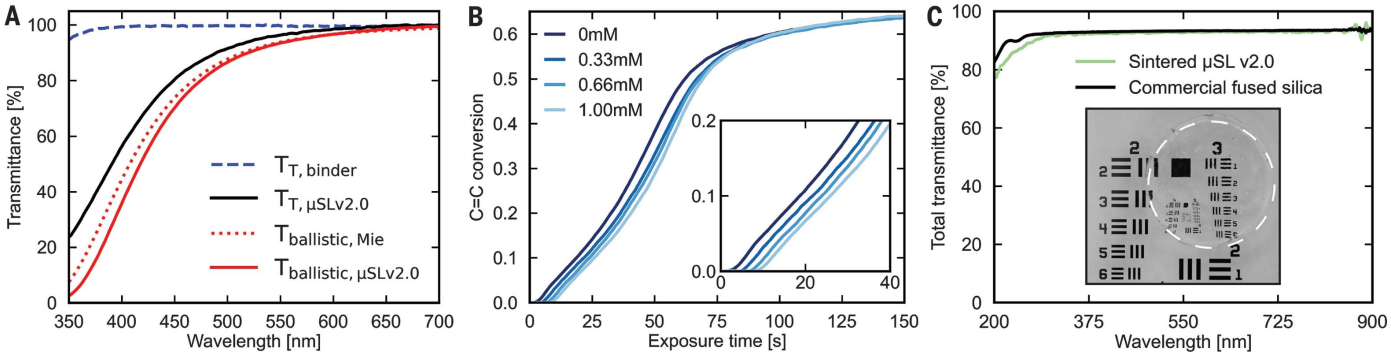

Fig. 2. Nanocomposite and sintered silica material characterization. (**A**) Binder (nanocomposite without silica) $T_{T,binder}$ and μSL v2.0 (with silica) transmittance spectra, where $T_{T,\ \mu SLv2.0}$ is total transmittance, $T_{ballistic,\ \mu SLv2.0}$ is the ballistic (collimated) component, and $T_{ballistic,\ Mie}$ is the transmittance estimated by Mie theory. (**B**) UV FTIR measurement of carbon-carbon double-bond conversion as a function of exposure time and concentration of TEMPO. An increased induction period is observed with increased TEMPO concentration. (**C**) Total transmittance spectra of micro-CAL–printed and sintered μSL v2.0 disk and commercial fused silica coverslip. The inset image shows qualitatively the optical transparency of a printed circular disk (inside the dashed circle) in front of a US Air Force (USAF) resolution target. See (*20*) for experimental details. (**D** and **E**) Scanning electron microscope (SEM) micrographs of cube cages printed and developed with 0 and 1 mM TEMPO, respectively. Scale bars are 200 μm.

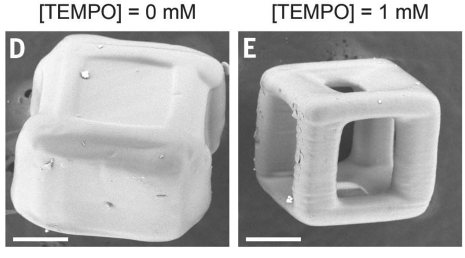

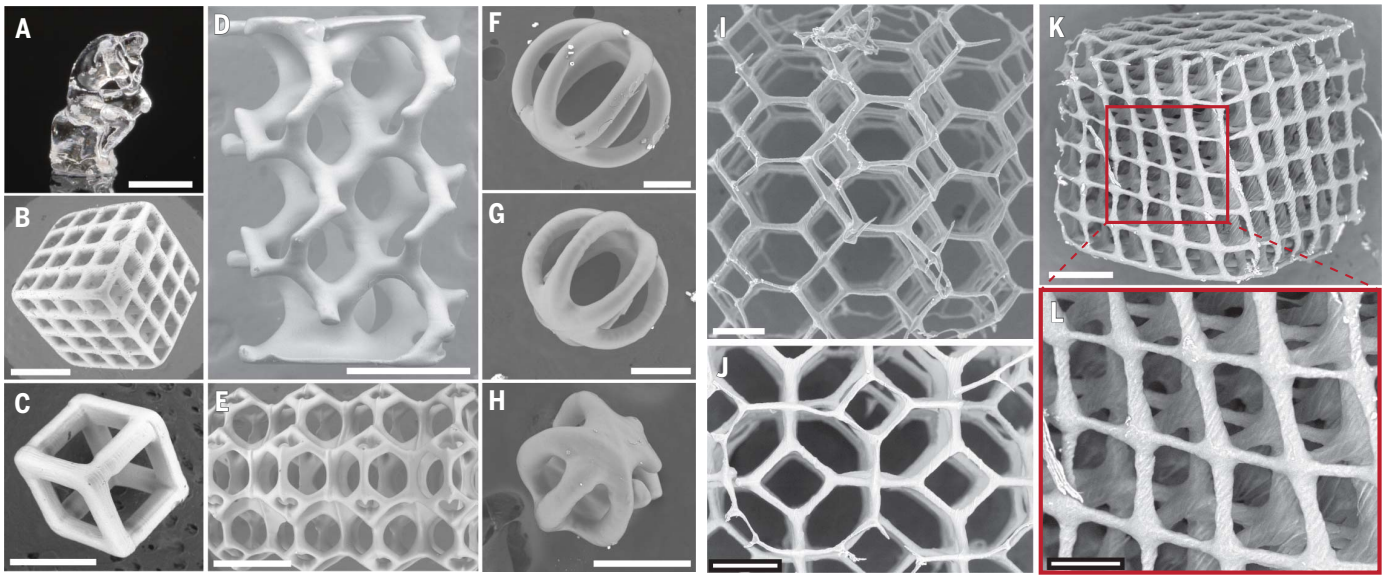

Fig. 3. CAL-printed glass structures. (**A** to **L**) Shown are Rodin's *The Thinker* (A), cubic lattice structures [(B) and (C)], a skeletal gyroid lattice with minimum positive feature size of 50 μm (D), a tetrakaidecahedron lattice (E), and spherical cage structures with minimum positive feature sizes of 75 (F), 60 (G), and 50 μm (H), respectively. Also shown are tetrakaidecahedron lattices [(I) and (J)] and a cubic lattice printed in monomeric photopolymer with a minimum positive feature size of 20 μm in each [(K) and (L)]. The images are a photograph in (A) and SEM micrographs in (B) to (L). Scale bars are 1 mm [(A) to (E)], 200 μm [(F) to (H)], 250 μm [(I) and (J)], 500 μm (K), and 100 μm (L).

and had a negligible effect on the kinetics of polymerization and the maximum degree of conversion.

The sharply nonlinear relationship between conversion and exposure dose provided by TEMPO substantially increased the lithographic contrast of the resin, thereby improving the feature modulation of the micro-CAL process. Increasing the TEMPO concentration reduced the degree of conversion in regions surrounding the printed object and inside internal voids and interstitial regions within the object (fig. S21). We show an example of such improvement using a particular set of digital light projections (Fig. 2, D and E). With TEMPO, conversion inside the void of the cubic cage was reduced, and the removal of uncured material was more easily achieved than in the nanocomposite without TEMPO (*20*). This improvement enabled fabrication of diverse geometries with positive feature sizes as low as 50 μm in the μSL v2.0 material (Fig. 3). In pure monomeric resin precursors, we achieved substantially smaller positive feature sizes as low as 20 μm (Fig. 3, I to L). We attribute this resolution enhancement for polymeric structures to the absence of solid nanoparticles, which results in easier development owing to lower resin precursor viscosity, a less brittle green state, and less light scattering (*20*).

Synthetic microstructured cellular materials have found use in a variety of fields, including photonics, energy, bioengineering, and desalination, as well as in high-temperature environments (*23*–*25*). Specifically, mechanical metamaterials, designed to exhibit mechanical properties that are unattainable by the bulk material—for example, a negative Poisson ratio—are emerging as an important area in AM because they often have a porous nature that is challenging to reproduce with conventional manufacturing techniques (*26*). In contrast with SLA, DLW, and fused filament fabrication, CAL builds objects volumetrically, which means that complex, low–relative density lattice and truss structures can be created in any orientation without supporting material (Figs. 3, B to D, and 4A). We fabricated tetrakaidecahedron lattices from transparent fused silica glass with strut elements of about 100 μm in diameter (Fig. 3E). For specific applications in which the orientation of the microstructure is critical, volumetric processing may prove useful because it eliminates defects due to layering that would be present in certain print orientations using other AM techniques.

We obtained surface-roughness metrics relevant to flaw-size characterization: arithmetic mean surface height, maximum valley depth, and root mean square surface gradient for rectangular beam specimens printed with micro-CAL and with SLA in vertical and horizontal orientations with respect to the build plate (fig. S13). We observed that micro-CAL produced significantly smaller and blunter defects and overall smoother surfaces (*20*). Three-point-bending mechanical testing showed that the difference between average fracture stress for different AM modalities was not statistically significant (Fig. 4A). However, the Weibull modulus for micro-CAL–printed beams was substantially higher than that for SLA-printed beams (Fig. 4B), showing that the fracture strengths of CAL-printed components are more tightly distributed (*27*).

To demonstrate the mechanical properties of a more complex micro-CAL–printed object, we fabricated a Howe truss (*28*), subjected it to three-point bend loading, and found that it achieved a fracture stress of 187.7 MPa (Fig. 4C and fig. S10). VAM limits the creation of microcracks and indentations that would otherwise compromise fracture strength. The mechanical characterization shows that micro-CAL can produce complex, high-strength fused silica components with superior reliability to other AM modalities. In the future, micro-CAL could be used to investigate new high-strength lattices that exploit silica's high intrinsic strength and strain at failure in the absence of large flaws (*29*).

Fused silica glass microfluidic devices offer many advantages over polymeric devices, including high resistance to temperature and harsh acids and organic solvents as well as high optical transmission over an extended UV, visible, and infrared range. However, conventional fabrication techniques such as planar lithographic processes require toxic fluoric etchants and are largely limited to two dimensions (*30*). With micro-CAL, we achieved rapid free-form fabrication of perfusable branched 3D microfluidics with low surface roughness, high transparency, and channel diameters and wall thicknesses as low as 150 and 85 μm, respectively (Fig. 4, D and E, and fig. S12). These properties show that micro-CAL has the potential to advance the fabrication

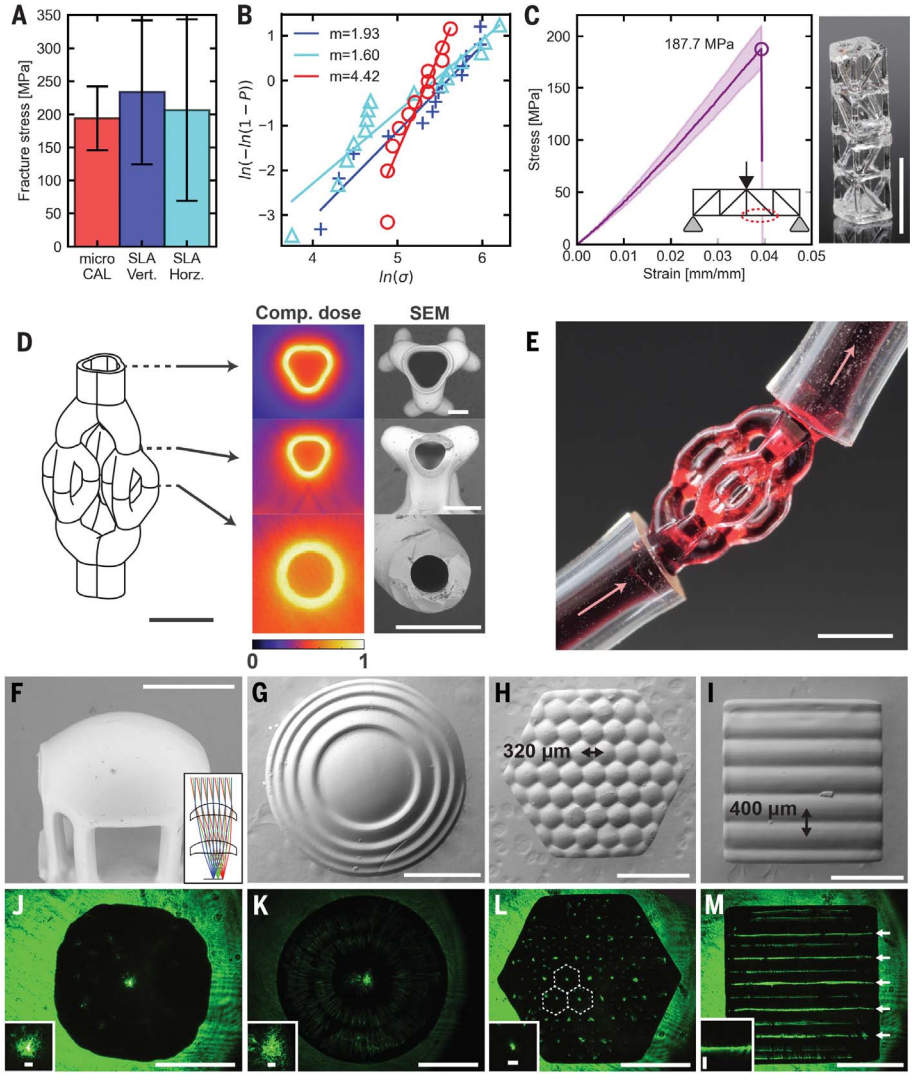

Fig. 4. Applications of glass CAL-printed microstructures. (**A**) Fracture stress of beams under flexure printed by micro-CAL and SLA in two different orientations: the long axis of the beam oriented vertically and horizontally with respect to the build plate. Data are means ± SD. *N* = 12, 14, and 16 for CAL, SLA vertical, and SLA horizontal, respectively. (**B**) Weibull modulus of the three types of printed beams, where *P* is the probability of failure and σ is the stress at failure. Color indicates print type and corresponds to the bar chart in (A). Each data point represents the fracture stress of an individual sample. (**C**) Three-point-bend test loading results (left) of a truss structure (right), where stress is the tensile stress in the bottom member as indicated by the red dashed oval in the schematic. The shaded region represents the bounded range of possible stresses due to variation in diameter of members. Scale bar is 2 mm. (**D**) Schematic of a trifurcated channel with normalized computational dose profiles (left) and SEM cross sections (right) at representative slices along a channel, revealing three levels of pore sizes: 750, 350, and 215 μm (top to bottom). Scale bars are 2 mm (schematic) and 500 μm (SEM micrographs). The color scale represents the normalized computational light dose. (**E**) Dyed liquid passed through the model demonstrates perfusability. Scale bar is 2 mm. (**F** to **I**) SEM micrographs of printed optical elements. (**J** to **M**) Point spread functions (PSFs) of the optical elements in (F) to (I) after focusing of 532-nm laser illumination. Insets show zoomed PSFs. Scale bars are 1 mm [(F) to (M)] and 50 μm [insets of (J) to (M)].

of microreactors, which are important for parallel drug screening and highly controlled flow synthesis (*3*).

The demand for more compact, lightweight, and high-quality cameras in consumer electronics and biomedical imaging pushes the development of advanced millimeter-scale optical systems. AM has enabled production of free-form refractive microlenses designed for specific applications, for example, foveated imaging. However, imaging elements made by layer-based techniques require post-processing such as polishing or coating to suppress the scattering induced by layer artifacts (*31*). With CAL, the 3D light dose possesses a radially and axially oriented gradient that has the effect of smoothening optical surfaces. We measured arithmetic mean line roughness (R_a) as low as 6 nm on as-fabricated lens surfaces using laser scanning confocal microscopy (fig. S17). We demonstrated printing of several refractive optical elements, including an air-spaced doublet aspheric lens optimized for operation at 532-nm wavelength, hexagonal and lenticular microlens arrays, and a spherical Fresnel lens (Fig. 4, F to I). The full-width half-maximum of the point spread function under collimated 532-nm illumination is less than 50 μm for each element. A low figure error in the range of 1 to 10 μm was achieved for spherical surfaces; however, a figure error of up to 60 μm persists for the aspheric lens surface, and imaging remains a challenge (figs. S15 and S16). These results suggest that although roughness is on par with commercial optics, figure error should be improved, perhaps by using in situ feedback and correction algorithms during printing (*17*, *32*).

The micro-CAL system we have developed enables manufacturing of structures with minimum feature sizes of 20 μm in polymer and 50 μm in fused silica, with excellent geometric freedom, low surface roughness, and high fracture strength and optical transparency in fused silica. Through optical engineering and specialized photopolymer development, we have established a glass fabrication framework that merges the facile processing of silica nanocomposites with layerless VAM and that could advance research in and industrial application of mechanical metamaterials, 3D microfluidics, and free-form optics.

REFERENCES AND NOTES

1. O. Solgaard, *Photonic Microsystems* (Springer, 2009).
2. B. C. Kress, I. Chatterjee, *Nanophotonics* **10**, 41–74 (2021).
3. F. Kotz, P. Risch, D. Helmer, B. E. Rapp, *Adv. Mater.* **31**, e1805982 (2019).
4. J. Luo *et al.*, *J. Manuf. Sci. Eng.* **139**, 061006 (2017).
5. C. Inamura, M. Stern, D. Lizardo, P. Houk, N. Oxman, *3D Print. Addit. Manuf.* **5**, 269–283 (2018).
6. K. C. Datsiou *et al.*, *J. Am. Ceram. Soc.* **102**, 4410–4414 (2019).
7. J. Lei, Y. Hong, Q. Zhang, F. Peng, H. Xiao, in *2019 Conference On Lasers Electro-Optics (CLEO)* (IEEE, 2019).
8. K. Sasan *et al.*, *ACS Appl. Mater. Interfaces* **12**, 6736–6741 (2020).
9. F. Kotz *et al.*, *Nature* **544**, 337–339 (2017).
10. I. Cooperstein, E. Shukrun, O. Press, A. Kamyshny, S. Magdassi, *ACS Appl. Mater. Interfaces* **10**, 18879–18885 (2018).
11. D. G. Moore, L. Barbera, K. Masania, A. R. Studart, *Nat. Mater.* **19**, 212–217 (2020).
12. F. Kotz *et al.*, *Adv. Mater.* **33**, e2006341 (2021).
13. J. Klein *et al.*, *3D Print. Addit. Manuf.* **2**, 92–105 (2015).
14. D. Yang, L. Liu, Q. Gong, Y. Li, *Macromol. Rapid Commun.* **40**, e1900041 (2019).
15. M. Shusteff *et al.*, *Sci. Adv.* **3**, eaao5496 (2017).
16. B. E. Kelly *et al.*, *Science* **363**, 1075–1079 (2019).
17. D. Loterie, P. Delrot, C. Moser, *Nat. Commun.* **11**, 852 (2020).
18. I. Bhattacharya, J. Toombs, H. Taylor, *Addit. Manuf.* **47**, 102299 (2021).
19. C. M. Rackson *et al.*, *Addit. Manuf.* **48**, 102367 (2021).
20. Materials and methods are available as supplementary materials.
21. E. T. Denisov, I. B. Afanas'ev, *Oxidation and Antioxidants in Organic Chemistry and Biology* (CRC Press, 2005).
22. C. C. Cook *et al.*, *Adv. Mater.* **32**, e2003376 (2020).
23. C. Maibohm *et al.*, *Sci. Rep.* **10**, 8740 (2020).
24. M. Thiel, M. S. Rill, G. von Freymann, M. Wegener, *Adv. Mater.* **21**, 4680–4682 (2009).

25. N. Sreedhar *et al*., *Desalination* **425**, 12–21 (2018).
26. X. Zheng *et al*., *Science* **344**, 1373–1377 (2014).
27. W. Weibull, *A Statistical Theory of the Strength of Materials* (Generalstabens Litografiska Anstalts Förlag, Stockholm, 1939).
28. W. Howe, Truss frame for bridges, US patent 1685 (1840).
29. C. R. Kurkjian, P. K. Gupta, R. K. Brow, *Int. J. Appl. Glass Sci.* **1**, 27–37 (2010).
30. C. Iliescu, H. Taylor, M. Avram, J. Miao, S. Franssila, *Biomicrofluidics* **6**, 016505 (2012).
31. X. Chen *et al*., *Adv. Mater.* **30**, e1705683 (2018).
32. C. C. Li, J. Toombs, H. Taylor, in *Proceedings of the Symposium on Computational Fabrication 2020 (SCF '20)* (Association for Computation Machinery, 2020).

ACKNOWLEDGMENTS

We thank the staff at the University of California (UC), Berkeley, Electron Microscopy Lab for advice in electron microscopy sample preparation and data collection. We thank P. Risch and M. Sanjaya for providing reference samples. We thank A. Warmbold for the thermogravimetric analysis measurement. We thank S. Kumar's lab at UC Berkeley for allowing use of the rheometer. We would like to thank the anonymous reviewers for their time and valuable critique. **Funding:** This work was funded by the National Science Foundation under cooperative agreement no. EEC-1160494 (J.T.T., C.C.L., H.K.T.); the European Research Council (ERC) under the European Union's Horizon 2020 Research and Innovation Programme (grant agreement nos. 816006 to M.L. and 825521 to S.J.); the Carl Zeiss Foundation as a part of the Research Cluster "Interactive and Programmable Materials (IPROM)"; the German Research Foundation (Deutsche Forschungsgemeinschaft, DFG) through the Centre for Excellence livMatS Exec 2193/1 – project number 390951807 (B.E.R.); the German Research Foundation (Deutsche Forschungsgemeinschaft, DFG) project number 455798326 (F.K.-H.); and the Lawrence Livermore National Laboratory Directed Research and Development program. The work was performed under the auspices of the US Department of Energy by Lawrence Livermore National Laboratory under contract DE-AC52-07NA27344 (LLNL-JRNL-826682) (C.C.C.).

Author contributions: Conceptualization: J.T.T., F.K.-H., H.K.T.; Methodology: J.T.T., M.L., F.K.-H.; Investigation: J.T.T., M.L., C.C.C., S.J., C.C.L.; Visualization: J.T.T.; Funding acquisition: H.K.T., F.K.-H., B.E.R.; Project administration: H.K.T., F.K.-H., J.T.T.; Supervision: F.K.-H., H.K.T., B.E.R.; Writing – original draft: J.T.T.; Writing – review and editing: All authors. **Competing interests:** H.K.T. holds US patent 10,647,061 relating to computed axial lithography. B.E.R. and F.K.-H. hold US patent 10,954,155 B2 relating to the silica nanocomposite material described in this paper. F.K.-H. and B.E.R. are co-founders of, and have an equity interest in, Glassomer GmbH. The authors declare that they have no other competing interests. **Data and materials availability:** All data are available in the main text or the supplementary materials. Code used to analyze and visualize data is available upon request.

SUPPLEMENTARY MATERIALS

science.org/doi/10.1126/science.abm6459
Materials and Methods
Supplementary Text
Figs. S1 to S23
Tables S1 to S9
References (*33*–*46*)

30 September 2021; accepted 23 February 2022
10.1126/science.abm6459